Nanoscale

ROYAL SOCIETY OF CHEMISTRY

PAPER

View Article Online
View Journal | View Issue

Check for updates

Cite this: *Nanoscale*, 2025, **17**, 12187

Tuning lipid nanocarrier mechanical properties to improve glioblastoma targeting and blood brain barrier penetration†

Ana Robles-Fernández, ‡[a,b] Daniel Jiménez-Boland,‡[a,b] Alberto Leon-Cecilla, [b,c] Martín Villegas-Montoya,[b,e] José Ángel Traverso,[a] Miguel A. Cuadros,[a] Antonio Martín-Rodríguez,[b] Modesto T. Lopez-Lopez, [b,c] Mattia Bramini, *‡[a] Carmen Lucía Moraila-Martínez*‡[d] and Paola Sánchez-Moreno*‡[b]

Nanocarrier lipid systems (NLSs) have emerged as versatile platforms for diagnostic and therapeutic applications, including drug delivery, gene therapy, and vaccine development. Recent advancements highlight their potential in targeting infectious diseases and treating pathological conditions like tumors, largely due to their ability to effectively encapsulate and deliver therapeutic agents. This study focuses on the synthesis and characterization of NLSs with varying lipid compositions to understand their physicochemical and mechanical properties, which are crucial for their performance in biomedical applications. NLSs were prepared using a solvent displacement method, resulting in formulations with different ratios of olive oil and stearic acid. These formulations were characterized to determine their size, polydispersity index, and surface charge. Dynamic Light Scattering and Nanoparticle Tracking Analysis revealed that the size of the NLSs increased with higher stearic acid content. The NLSs demonstrated stability across a range of pH levels and in cell culture medium. The biomolecular corona formation and its impact on surface charge were also evaluated, showing significant effects on NLS stability. Mechanical properties, including rigidity and deformability, were assessed using Atomic Force Microscopy and rheological tests. The study found that increasing stearic acid content enhanced NLS rigidity and adhesion strength, which is crucial for their behaviour in biological systems such as blood circulation, tumor targeting, and cellular uptake. Biological evaluations demonstrated that these mechanical properties significantly influenced bio-interactions. Softer NLSs with a pure olive oil core displayed enhanced translocation across an *in vitro* blood–brain barrier model, underscoring their potential for drug delivery to the brain. Conversely, glioblastoma cell uptake studies revealed that the more rigid NLSs were internalized more efficiently by U87-MG cells, suggesting a role for stiffness in cellular entry. These findings provide insights into optimizing NLSs for specific therapeutic applications, particularly in overcoming barriers like the blood–brain barrier and targeting cerebral diseases.

Received 6th March 2025,
Accepted 14th April 2025

DOI: 10.1039/d5nr00984g

rsc.li/nanoscale

Introduction

Nanocarrier lipid systems (NLSs) have emerged as a crucial platform in modern diagnostic and therapeutic applications, revolutionizing drug delivery, gene therapy, and vaccine development.[1] Their versatility has been particularly evident in tackling infectious diseases, notably in mRNA-based vaccines against SARS-CoV-2,[2] where they enable efficient intracellular delivery and a robust immune response.[3] Moreover, NLSs demonstrate great potential in oncology and other pathological conditions,[4] owing to their exceptional ability to encapsulate and effectively transport therapeutic agents. Additionally, their cost-effectiveness and scalability make them an attractive

---

[a] *Universidad de Granada, Departamento de Biología Celular, E-18071 Granada, Spain. E-mail: mbramini@ugr.es*
[b] *Universidad de Granada, Departamento de Física Aplicada, E-18071 Granada, Spain. E-mail: paolasm@ugr.es*
[c] *Instituto de Investigación Biosanitaria Ibs.GRANADA, E-18014 Granada, Spain*
[d] *Universidad de Granada, Departamento de Electrónica y Tecnología de Computadores, E-18071 Granada, Spain. E-mail: cmoraila@ugr.es*
[e] *Universidad Autónoma de Sinaloa, Facultad de Biología, 80040 Culiacán, Mexico*

† Electronic supplementary information (ESI) available. See DOI: **https://doi.org/10.1039/d5nr00984g**

‡ These authors contributed equally.

option for widespread medical applications.[5] Beyond their potential as robust delivery tools, NLSs present extremely low toxicity, offering high biocompatibility and biodegradability due to their lipid-based composition.[6,7] Their components are generally classified as GRAS or FDA-approved, ensuring a high safety profile for NLSs.

Depending on the lipid composition, NLSs can take various forms, such as solid lipid nanoparticles (SLNs), nanostructured lipid nanocarriers (NLCs), and liquid lipid nanoparticles (LLNs), each offering distinct properties and advantages. LLNs enable the ability to carry large quantities of hydrophobic drugs in the dispersed phase and protect them from degradation but may face drug leakage.[7,8] Conversely, SLNs offer exceptional stability, allowing for long-term storage and controlled agent release, making them an attractive choice for drug delivery.[9] However, the crystalline structure of the lipid core can be a drawback, as the crystallization during the synthesis sometimes results in low drug encapsulation and loading efficiency. Finally, NLCs consist of a matrix made from a combination of solid and liquid lipids. Compared to SLNs, NLCs offer the advantage of a higher capacity for loading active compounds.[6] Despite the promising outlook, a comprehensive understanding of how the mechanical properties of NLSs might influence their biological interactions with living systems, such as cellular uptake and transport across biological barriers, still needs to be fully explored. The mechanical properties of nanoparticles (NPs) play a pivotal role in determining their behaviour within biological systems influencing blood circulation, tumor targeting, biodistribution, tumor penetration, accumulation, and cellular internalization.[10]

Softer NPs remain longer in blood circulation than stiffer counterparts because of their distinct phagocytosis profile: their ability to deform under macrophage-induced forces reduces susceptibility to sequestration into the macrophages, extending circulation time.[10] Furthermore, their deformability enables them to traverse pores and fenestrations typical of the vascular endothelium structure (paracellular pathway), while maintaining structural integrity. In contrast, stiffer NPs, with limited deformability, tend to accumulate in the spleen, leading to shorter circulation.[11] Efforts to enhance tumor targeting suggest that reducing NP elasticity might minimize macrophage uptake, thereby improving tumor accumulation.[12] The malleability of NPs also plays a critical role in tumor penetration. More elastic NPs exhibit enhanced penetration capabilities, as their superior deformability allows them to navigate intercellular spaces and penetrate deeper into tumor regions. Conversely, stiffer NPs, with limited deformability, tend to remain confined to the tumor periphery.[12] Finally, cell adhesion is primarily driven by ligand–receptor interactions between NPs and cell membranes. Softer NPs display a heightened propensity for multivalent binding than stiffer counterparts due to their ability to deform into a flattened configuration, enhancing adhesion.[13,14]

Thus, understanding, regulating, and optimizing the mechanical properties of NPs is crucial for developing advanced nanomedicine tools for theranostics. The physical and mechanical characteristics of NPs significantly influence their interaction with cells and their ability to cross biological barriers.[15] In particular, rigidity plays a key role in determining cellular uptake and biodistribution, as well as the ability to navigate biological environments. More deformable NLSs can more effectively cross membranes and withstand mechanical forces, enhancing their potential for targeted delivery. However, despite extensive research on NP mechanics, a comprehensive comparative study on how the mechanical properties of NLSs affect cell uptake and barrier translocation remains lacking. Addressing this knowledge gap is crucial, particularly for applications requiring NLS to traverse biological barriers like the blood–brain barrier (BBB) to target brain diseases such as glioblastoma multiforme (GBM). The BBB, a highly selective barrier safeguarding the central nervous system, presents a major challenge for brain drug delivery. Developing NLSs with optimized mechanical properties to enhance BBB crossing while efficiently encapsulating high drug concentration remains a critical goal.

This study aimed to obtain NLS systems with tuneable rigidity by adjusting the ratio of liquid and solid lipids in the core (olive oil and stearic acid, respectively). We conducted a comprehensive characterization of their physicochemical and mechanical properties to better understand their behaviour and stability over time and in complex biological media. Additionally, we investigated their *in vitro* cellular uptake and transport across a human *in vitro* BBB model to assess their potential as efficient drug delivery carriers. The findings of our study contribute to the advancement of NLS-based drug delivery systems, particularly for targeting cerebral diseases such as GBM. We confirmed that lipid core composition significantly influences the physicochemical properties of NLS, with stearic acid-only cores exhibiting instability, whereas olive oil-based cores demonstrated promising biological potential, especially for BBB crossing. Additionally, cellular uptake studies revealed that slightly stiffer particles containing a small percentage (10%) of stearic acid in the core were taken up more efficiently. These findings highlight the importance of selecting an appropriate lipid composition based on the intended application, as it directly affects NLS biointeractions. Protocol standardization and surface functionalization may pave the way for innovative therapies, ultimately advancing precision medicine and improving treatment outcomes for challenging medical conditions.

Results and discussion

Nanocarrier lipid systems preparation and characterization

As detailed in the Materials and methods section, five different NLS formulations were synthesized by modifying a well-established solvent displacement protocol.[7] The NLSs are composed of a mixture of phospholipids, Pluronic F-68, and varying proportions of olive oil and stearic acid, resulting in the following formulations: 100 : 0, 90 : 10, 70 : 30, 50 : 50, and 0 : 100 (Fig. 1A). In these ratios, the 100 : 0 formulation con-

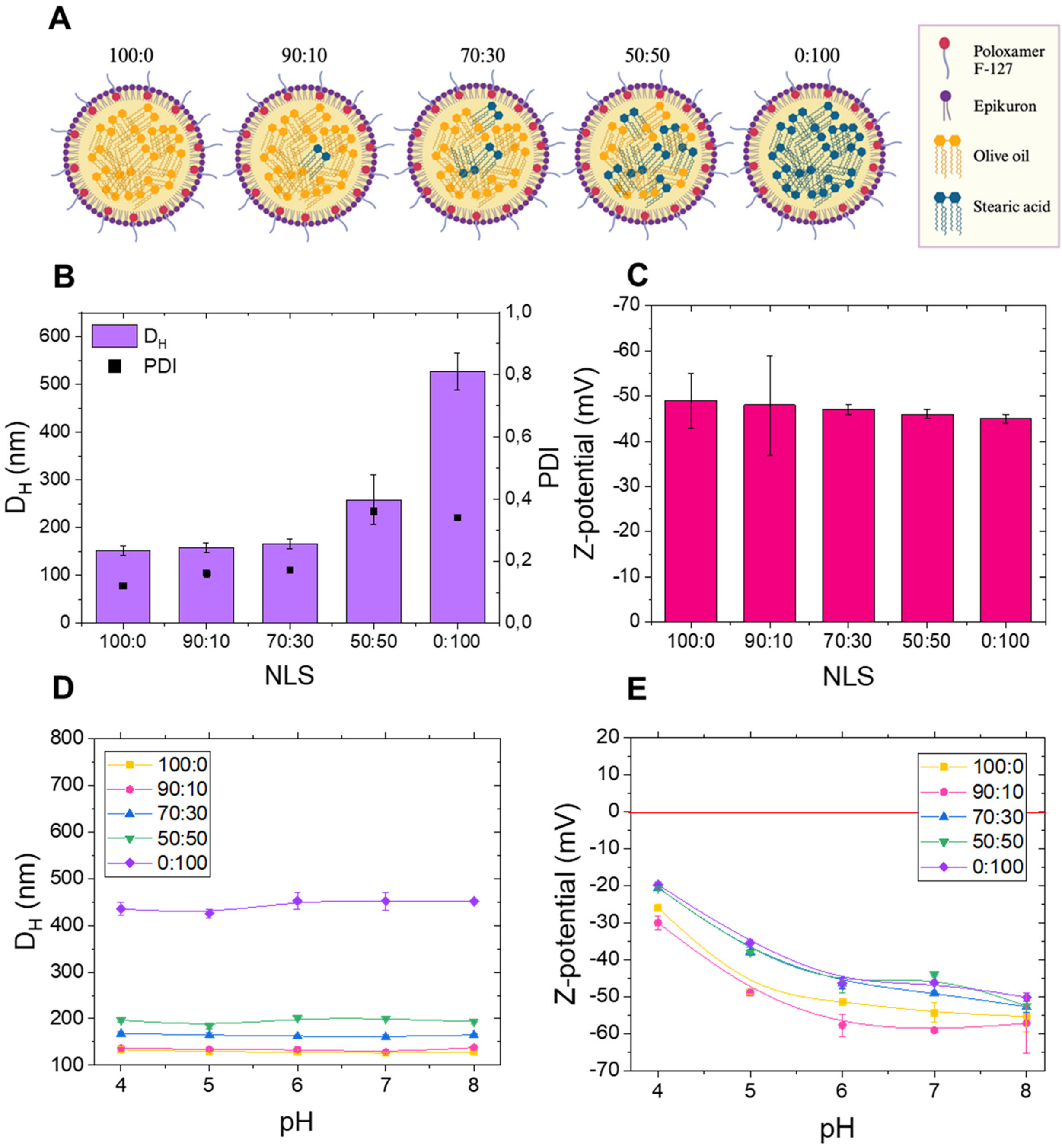

Fig. 1 Characterization of the NLSs. (A) Schematic representation of the five NLSs with varying proportions of olive oil and stearic acid. (B) Hydrodynamic mean diameter (D_H) and polydispersity (PDI) of the five systems. (C) *Z*-Potential of the different NLSs in Milli-Q water. (D) Hydrodynamic mean diameter (D_H) of NLSs in different buffers. (E) *Z*-Potential of NLSs in different buffers data are represented as the average of 3 independent replicates ± SD.

tains only olive oil as the core, while the 0 : 100 formulation contains only stearic acid. The various ratios of olive oil to stearic acid in the NLS compositions were thoroughly investigated through extensive physicochemical characterization in different aqueous solutions.

The hydrodynamic diameter (D_H) of the 100 : 0, 90 : 10, 70 : 30, 50 : 50, and 0 : 100 NLSs was determined by dynamic light scattering (DLS) as 151 ± 9, 158 ± 10, 166 ± 9, 258 ± 52, and 527 ± 38 nm, respectively (Fig. 1B and Table S1†). These results are consistent with previous reports for distinct nanoemulsions synthesized using the solvent displacement technique.[16,17] Furthermore, the Polydispersity Index (PDI) values for all five NLSs were detected as 0.12 ± 0.05, 0.16 ± 0.04, 0.17 ± 0.08, 0.36 ± 0.11, and 0.34 ± 0.05, as shown in Fig. 1B and Table S1.† These results display no significant size differences among the 100 : 0, 90 : 10 and 70 : 30 systems, indicating that the proportions of olive oil and stearic acid tested did not affect NLS dimensions. Additionally, 100 : 0, 90 : 10, and 70 : 30 NLSs all exhibit low polydispersity index (PDI < 0.2), suggesting that they are monodisperse systems when analyzed immediately after synthesis. The size of these three NLSs falls within the optimal range of size (<200 nm) for biomedical applications, as they could extravasate into tumor tissues, enabling effective concentration and delivery of therapeutic cargo through the enhanced permeability and retention (EPR) phenomenon.[18] In contrast, the 50 : 50 and 0 : 100 NLSs show a significant increase in particle size, with the 0 : 100 formulation (composed solely of stearic acid) having the largest diameter. Additionally, 50 : 50 and 0 : 100 NLSs have a PDI > 0.3, indicating a polydisperse distribution and suggesting the possible presence of particle aggregation. Table S1† summarizes the diameters of all the NLSs synthesized and Fig. S1† graphically represents the size distributions obtained through Nanoparticle Tracking Analysis (NTA). The comparison between DLS and NTA data confirmed that, as the proportion of stearic acid in the lipid core increased, a notable rise in particle size was observed. No differences in dimensions were observed for the 100 : 0, 90 : 10, and 70 : 30 NLSs, while the 50 : 50 and 0 : 100 NLSs showed an increase in size in both DLS and NTA measurements. In the case of the 0 : 100 NLSs, the hydrodynamic diameter determined by NTA is expressed as the weighted average diameter (Fig. S1B†), although distinct populations are observed in this nanosystem. One population shows a similar D_H to the 100 : 0 system but with a broader peak, and two additional populations exhibit higher D_H values compared to the other NLSs.

Although some NPs could still be considered acceptable for drug delivery applications, this system is the most polydisperse, which could interfere with its *in vitro* and *in vivo* performance. The slight variations in diameter values from DLS and NTA can be attributed to the different methodologies and algorithms employed by these techniques. Finally, a comparative analysis of the surface charge of the NLSs (*Z*-potential) revealed no significant differences among the synthesized NLSs, with values being strongly negative (>−40 mV) (Fig. 1C and Table S1†). This suggests that variations in lipid proportions within the NLS core do not influence the surface charge. Therefore, the observed *Z*-potential is primarily attributed to the surfactants used in NLS preparation, which play a crucial role in stabilizing the NLSs and imparting electrical charge. Notably, these results are consistent with those reported by Sánchez-Moreno *et al.*[19] when working with NLSs composed of olive oil in the core and the same surfactants. We then implemented the characterization of NLSs by conducting an exhaustive evaluation of the D_H and *Z*-potential at different pH values, ranging from pH 4 to pH 8 (Fig. 1D and E). All NLSs exhibited a negative *Z*-potential in the pH range investigated, and the dimension of NLSs was found to be stable at all pHs. Once again, as the percentage of stearic acid in the synthesis increased, the D_H of the NLSs also raised, indicating a direct relationship between the composition of the NLS core and their size/aggregation state. These results imply high colloidal stability of all NLSs at physiological pH, with a *Z*-potential exceeding 30 mV (in absolute value).[20] A common pattern was observed in *Z*-potential values for all NLSs, wherein an increase in pH led to a more negative *Z*-potential, a typical characteristic of colloidal particles with weak acid groups.[16,19] This behaviour can be attributed to the surface-charged groups of Epikuron 145 V. Previous studies have also reported a similar trend in *Z*-potential measurements, showing lower absolute values at acidic pH, with an increase at neutral and basic pH.[19]

In summary, the results indicate that while the NLSs maintain a negative *Z*-potential and exhibit colloidal stability across a wide pH range, only the formulations with lower stearic acid content (100 : 0, 90 : 10, and 70 : 30) have sizes suitable for drug delivery applications. In contrast, the 50 : 50 and 0 : 100 nanosystems, despite maintaining their size across different pH levels, including physiological pH, are not appropriately sized for such applications. Since 50 : 50 and 0 : 100 NLSs exhibited some aggregation associated with high PDI values (Fig. 1B), only 100 : 0, 90 : 10, and 70 : 30 NLSs were selected to continue with the following experiments.

Colloidal stability over time, critical coagulation concentration (CCC) and critical stabilization concentration (CSC)

Colloidal stability over time is a crucial factor when evaluating the suitability of a nanosystem for biomedical applications. Aggregation over time compromises its bioavailability, transport capacity, and therapeutic response. Therefore, ensuring long-term colloidal stability is essential to guarantee predictable and safe behaviour in biological environments. Thus, the colloidal stability of the NLSs was explored in Milli-Q water and phosphate-buffered saline (PBS) (Fig. 2A and B). The 70 : 30 NLSs exhibited a significant increase in size over time compared with the 100 : 0 and 90 : 10 systems after 10 days in water with the aggregation being even more pronounced in PBS. These findings suggest that NLSs may undergo changes in size over time, which become more pronounced when the ionic strength increases, as in the case of PBS. The proportion of olive oil and stearic acid influences the extent of this change, as demonstrated by the fact that the 100 : 0 and 90 : 10 formulations, which have a higher concentration of olive oil in the core, were more stable than the 70 : 30 formulation in both the media investigated.

For a complete understanding of the behaviour of colloidal particles, it is necessary to explore the conditions under which the NLSs initiate coagulation and start forming aggregates. The NLS critical coagulation concentration (CCC) and critical stabilization concentration (CSC) were determined, which are fundamental parameters in colloidal stability studies. The CCC value is associated with destabilization processes and indirectly provides information on the surface charge density of the NPs; thus, a low CCC indicates low stability due to a low surface charge density. Conversely, the CSC value – defined as the minimum salt concentration at which the system begins to re-stabilize upon increasing salinity – is related to surface hydrophilicity. This re-stabilization phenomenon at high salt

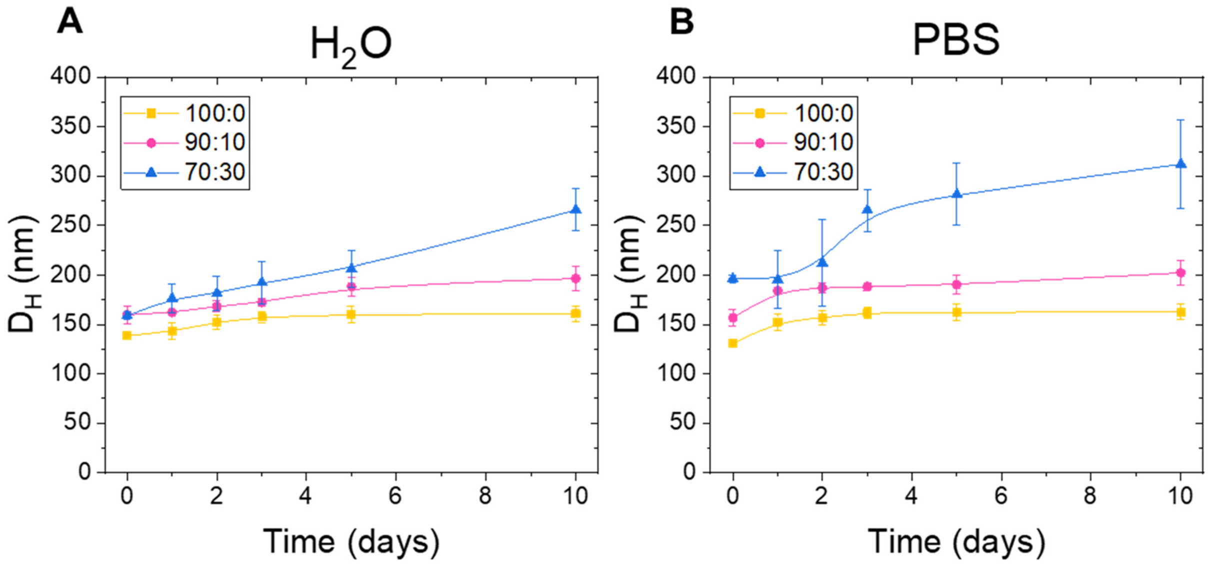

C

NLS	NaCl (mM)		CaCl₂ (mM)	
	CCC	CSC	CCC	CSC
100:0	stable	stable	74	88
90:10	stable	stable	65	85
70:30	stable	stable	42	*

Fig. 2 Colloidal stability of the NLS. (A) Evaluation of hydrodynamic mean diameter (D_H) over time in Milli-Q water (B) Evaluation of hydrodynamic mean diameter (D_H) over time PBS. In A and B data are represented as the average of 3 independent replicates ± SD. (C) Assessment of critical coagulation concentration (CCC) and critical stabilization concentration (CSC) of the NLS in NaCl and $CaCl_2$. *N/A.

concentrations is well-known in hydrophilic colloidal systems and is governed by hydration forces.[21] Thus, NLS stability was evaluated in the presence of a monovalent salt (NaCl) and a divalent salt ($CaCl_2$) and the CCC and the CSC were determined using visible light spectrophotometry. The summarised results are presented in Fig. 2C. Interestingly, all NLSs exhibited stability in NaCl, indicating their ability to withstand coagulation even at salt concentrations exceeding 500 mM. These findings suggest that the electrostatic repulsion between the particles was sufficient to maintain a satisfactory dispersion, preventing aggregation and the formation of larger structures. The observed stability under high salt concentration is a promising characteristic for the potential applications of NLSs in biomedicine, where the biological environment is rich in ionic species. Furthermore, the ability to avoid coagulation ensures the integrity of the NLSs and their potential functionality, which is crucial for their performance as drug delivery carriers. CCC and CSC were then measured in the presence of $CaCl_2$ The decreasing CCC with increasing stearic acid concentration indicates a lower stability of the NLSs, likely due to the reduced surface charge density associated with the larger particle sizes. This trend highlights the significant impact of stearic acid concentration on the colloidal stability and aggregation behaviour of the NPs. In addition, in systems with higher amounts of olive oil (100 : 0 and 90 : 10), CSC values were observed (88 and 85 respectively), indicating that the system re-stabilizes at higher salt concentrations. This behaviour is associated with a more hydrophilic surface. The increased presence of hydrophilic molecules, such as the hydrophilic segments of the Pluronic F68 in the smaller systems likely contributes to this effect. The larger surface area of these systems, due to their smaller particle size, provides more opportunities for the hydrophilic molecules to interact with the surrounding aqueous environment, enhancing the system's ability to re-stabilize. This correlation suggests that as the amount of olive oil increases, the system becomes more hydrophilic and better able to maintain stability in high-salinity conditions.

Characterisation of mechanical properties of NLSs *via* atomic force microscopy

The mechanical properties of NLSs are crucial for their biomedical applications, particularly in drug delivery and cellular uptake. In this study, atomic force microscopy (AFM) in force spectroscopy mode was employed to map the nanomechanical properties of NLSs formulated with different proportions of olive oil and stearic acid. The use of AFM in this context is critical, as it allows for precise characterization of mechanical properties at the nanoscale level, offering a unique advantage in understanding how lipid composition modulates NLS rigidity. These insights are pivotal for optimizing NLS formulations tailored to specific therapeutic applications, such as crossing the blood–brain barrier or improving tumor targeting. Previous studies have demonstrated that the rigidity of nanocarriers plays a crucial role in their ability to penetrate biological barriers and resist mechanical deformation during circulation, both of which are essential for drug delivery efficacy.[22,23]

Fig. 3A shows the AFM topographical images of NLS formulations (100 : 0, 90 : 10, 70 : 30). These images reveal significant morphological differences as the lipid composition varies. The NLSs with higher stearic acid content (90 : 10 and 70 : 30) exhibit a more compact and rigid structure compared to the 100 : 0 formulation, which shows more dispersed and softer characteristics. This qualitative observation is supported by the quantitative nanomechanical measurements discussed below.

As seen in Fig. 3B and C, the mechanical properties of NLSs exhibit a clear trend correlated with stearic acid content. The elastic modulus, which measures the rigidity of the particles, increases from 4.8 N m^{-2} in the 100 : 0 formulation to 5.8 N m^{-2} in the 70 : 30 formulation, indicating a marked increase in rigidity as the proportion of stearic acid increases. Similarly, adhesion forces, which are indicative of how the NLSs interact with surfaces, increase from 13.1 nN in the 100 : 0 formulation to 17.0 nN in the 70 : 30 formulation. These increases in both elastic modulus and adhesion strength suggest that the incorporation of stearic acid significantly alters the mechanical properties of the NLSs, making them stiffer and more adhesive.

Our findings, which demonstrate an increase in both rigidity and adhesion of nanocarrier lipid systems (NLSs) with higher stearic acid content, align with the work of Hui *et al.*[10] They showed that greater nanoparticle rigidity enhances circulation stability by reducing premature clearance. This suggests that the increased rigidity observed in our NLS formulations may indeed improve stability in the bloodstream, prolonging circulation time. However, as Hui *et al.* also noted, excessive rigidity can hinder tumor tissue penetration, underscoring the

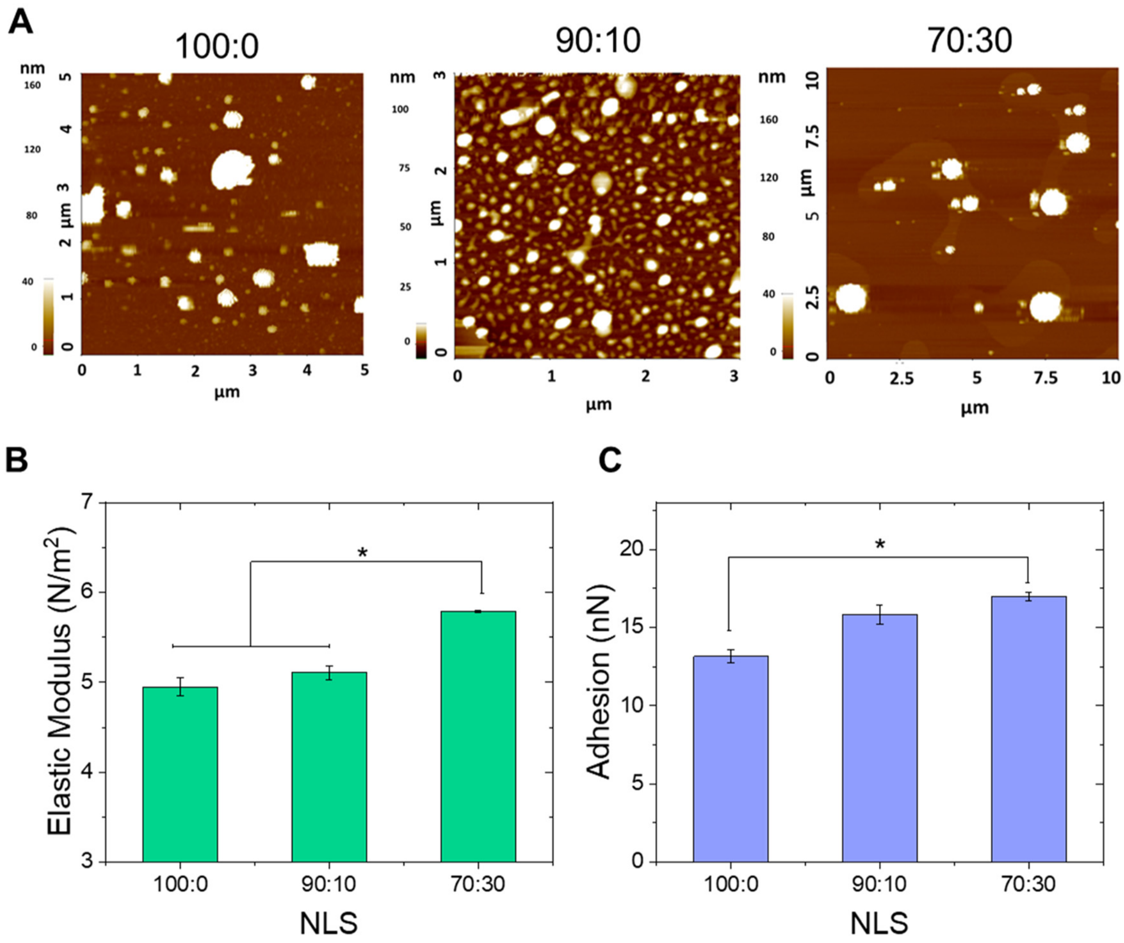

Fig. 3 Characterization of NLS mechanical properties. (A) Topographic images of NLS (100 : 0, 90 : 10, and 70 : 30). The *z*-range of the AFM images is indicated on the colour bar. (B) Elastic modulus and (C) adhesion of the NLSs measured by Atomic Force Spectroscopy (AFM) in Pin-point mode. One-way ANOVA followed by Tukey's *post hoc* test showed significant differences between all groups ($p < 0.05$) $n = 30$.

need to balance mechanical properties to optimize nanoparticle performance for specific biomedical applications. Thus, our results highlight the importance of tailoring the rigidity and elasticity of NLSs to the targeted biological environment. For instance, while increased rigidity may improve blood circulation, it could limit cellular uptake in some contexts. Achieving an optimal balance between these properties is crucial for enhancing the therapeutic efficacy of nanocarriers. Studies further support that softer nanoparticles may improve tumor penetration, whereas stiffer particles can ensure prolonged circulation and better tissue accumulation.[10,24,25] Moreover, although anticancer drugs were not encapsulated in the present formulations, these systems are designed for potential application as drug delivery vehicles, making it essential to consider that drug incorporation may alter the physicochemical characteristics of the SLNs. The incorporation of therapeutic agents, particularly hydrophobic drugs such as temozolomide (TMZ) used in brain cancer treatment, might significantly modulate the physicochemical and mechanical properties of NLSs, influencing parameters such as rigidity, adhesion strength, and colloidal stability. For instance, Jeitler *et al.*[26] demonstrated that drug incorporation modifies the crystallinity and mechanical strength of nanostructured lipid carriers, impacting their biological interactions, while Beloqui *et al.*[27] reported changes in particle elasticity that affect mucosal adhesion and systemic distribution. Therefore, it is essential to consider the impact of drug encapsulation on NP behavior in future formulations and to characterize the NLSs after drug loading to ensure an accurate assessment of their functional properties and therapeutic potential.

Characterization of mechanical properties of NLSs through rheology

In this study, rheology tests were performed to characterize the viscoelastic properties of NLSs in suspension, representing a significant advancement in understanding the mechanical behaviour and flow characteristics of NLSs.

The shear stress (σ) as a function of the shear rate ($\dot{\gamma}$) is presented in Fig. 4A. From these data and those of Fig. 4B, it can be concluded that the three analyzed systems show similar shear-thinning rheological behaviour. It is important to note that the presence of stearic acid in the core of the particles affects the flow behaviour of the whole system, with changes becoming more pronounced as its concentration increases. In order to have a quantitative comparison between the three plotted curves, they were fitted using the empirical Herschel–Bulkley equation for non-Newtonian fluids:

$$\sigma = \sigma_0 + K\dot{\gamma}^n$$

where σ_0 is the yield stress, K is the consistency index, and n the flow index. This equation is only valid for values of the stress higher than σ_0 ($\sigma_0 < \sigma$).[28,29] The values of the parameters obtained from the fittings model are shown in Table 1.

The mentioned changes in the rheological behaviour are reflected in the value of σ_0, which increased with a higher presence of stearic acid. Considering that the surface of the particle does not change when the stearic acid is included, it seems that the changes in the flow are caused by differences in the mechanical properties of the particles, as presented in AFM measurements. In fact, the effect of particle softness on the rheology of particulate suspensions was studied by Mewis *et al.* (1989),[30] using suspensions of PMMA particles with a grafted poly (12-hydroxystearic acid) layer of varying relative thickness to core diameter as model systems. They found that the maximum packing density of the particles increased with particle softness, which affected the viscosity of the suspensions at high volume fractions (>0.4). Since we are studying similar volume fractions in the present work, it is evident that the differences observed in Fig. 4 may be due to the mechanical properties of the particles. Furthermore, in the three cases $n < 1$ that is characteristic of shear-thinning materials. It is important to note the obvious differences in the parameters between the three studied systems, which reflect the effect of the presence of the stearic acid on the overall properties of the dispersion and the particle itself.

The viscosity behaviour of the three NLS systems, presented in Fig. 4B, also shows the aforementioned shear thinning behaviour with a monotonic decrease in viscosity as the shear rate increases. The 70 : 30 system exhibits a higher flow resistance than the 90 : 10 and 100 : 0 systems, corroborating the effect of the stearic acid on the properties of the NLS and thereby of the suspension. Fig. 4C illustrates the relationship between the modulus of the complex viscosity (η^*) and the shear strain amplitude (γ), for the three NLS systems. The complex viscosity characterizes the flow behaviour of the system under oscillatory shear, being, in this case, a viscoelastic liquid.[29] The 90 : 10 and 70 : 30 systems exhibited higher values of this parameter, contrasting with the 100 : 0 system, which translates into higher values of the viscoelastic moduli when the stearic acid is present. Fig. 4D shows the viscoelastic moduli G' and G'' as a function of the angular frequency, where the 100 : 0 has the typical tendency of a liquid-like polymeric solution ($G'' > G'$, with G'' proportional to w, and G' to $\omega 2$) while 90 : 10 and 70 : 30 have a more exotic behaviour with both moduli exhibiting a similar tendency with ω.[31] In all cases, however, $G'' > G'$, as typical for a liquid-like sample. Also, in agreement with the trends previously discussed for shear stress and viscosity, the magnitudes of both G' and G'' increase from the 100 : 00 to the 70 : 30 systems as the stearic acid concentration increases, further corroborating the enhancement of rigidity with stearic acid content. These results underscore the relevance of lipid composition in determining the rheological performance of NLSs, aligning with previous studies highlighting lipid components' influence on lipid nanoparticles' mechanical properties.[29,32]

These findings provide valuable insights into the relationship between lipid composition and the viscoelastic properties of NLSs in suspension. Additionally, this study adds to the growing body of literature supporting the potential of rheological techniques for characterizing the mechanical properties of nanoparticle systems.[33] This research contributes to the comprehensive understanding of nanolipid behaviour by employing rheology as a tool for NLS characterization.

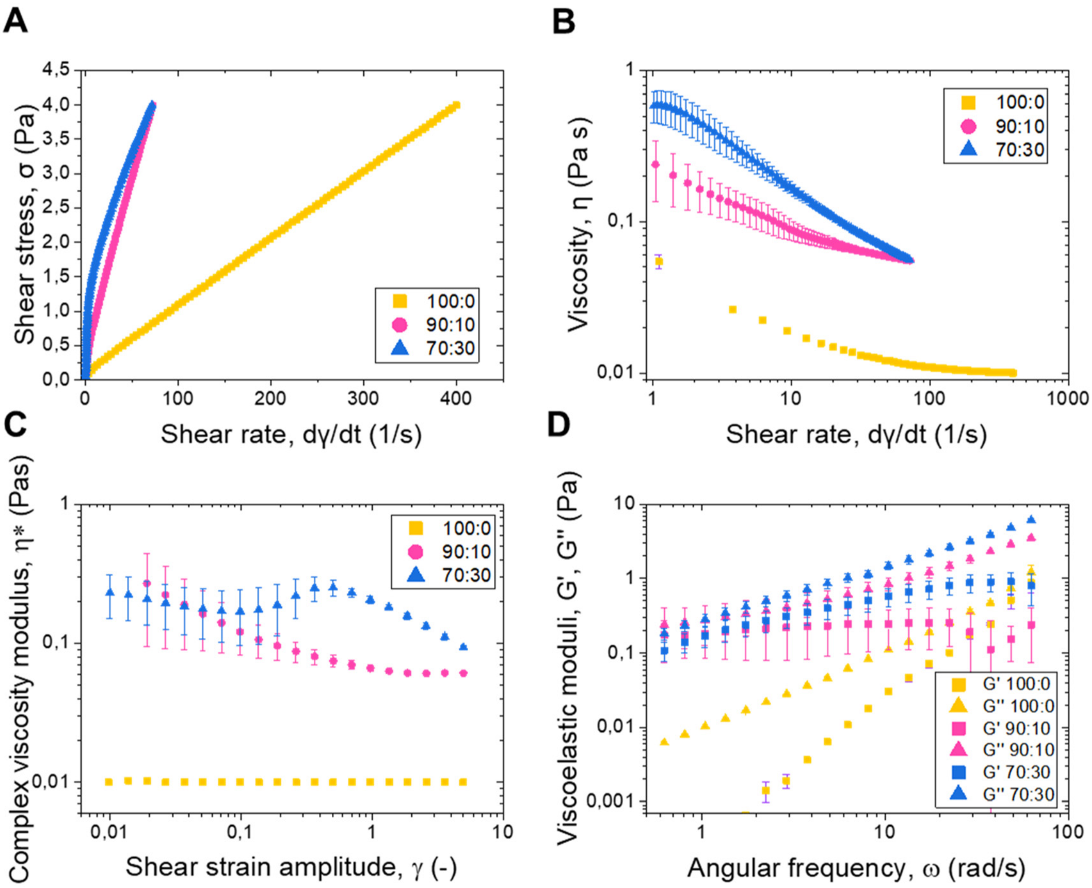

Fig. 4 Rheological characterization of the NLS. (A) Shear stress (σ) as a function of the shear rate ($\dot{\gamma}$). (B) Viscosity (η) as a function of the shear rate ($\dot{\gamma}$). (C) Relationship between the modulus of the complex viscosity (η^*) and the shear strain amplitude (γ). (D) Viscoelastic moduli G' and G'' as a function of the angular frequency $n = 3$.

Table 1 Parameter obtained from the fitting of the Herschel–Bulkley equation for each measured system

Parameter	σ_0 (Pa)	K (Pa·s^n)	n (−)	R^2
100 : 0	0.1030 ± 0.0014	0.01029 ± 0.00004	0.9910 ± 0.0007	1
90 : 10	0.229 ± 0.004	0.0820 ± 0.0008	0.8938 ± 0.0019	0.999
70 : 30	0.55 ± 0.03	0.256 ± 0.012	0.607 ± 0.009	0.998

Ultracentrifugation spin-down assay

This study introduces a pioneering assessment of the deformability of NLS using the ultracentrifugation spin-down method, inspired by the methodology proposed by Kong *et al.* (Fig. 5A).[34] This semi-quantitative assay allowed us to examine the relative differences in NLS deformation quickly and accessibly, which is particularly valuable for comparing various formulations in a relevant environment of fluid suspension under shear stress. Briefly, to simulate a biological barrier (specifically an endothelium), we chose to employ filter tubes with pore sizes based on the dimensions of discontinuous endothelial junctions present in critical structures such as the spleen and the blood–brain barrier (BBB), which range between 200 and 500 nm.[35,36] The results indicate that 100 : 0 NLSs possess a higher degree of deformability, as reflected in their superior ability to pass through the filter while 90 : 10 and 70 : 30 systems showed a progressively more reduced passage (Fig. 5B), and, therefore, less deformability. These findings align with the results obtained from the AFM analysis, clearly suggesting a correlation between NLS mechanical properties, such as deformability, and their capacity to pass through membrane pores. This centrifugation spin-down assay provides a valuable tool for researchers to gain deeper insights into the nanoscale carriers' physical characteristics, which in turn enhances the design of more effective drug-delivery nanoparticles in complex biological environments. The ability of NLSs to deform their structure and navigate through biological barriers is crucial for their successful application in targeted drug delivery and other biomedical applications.

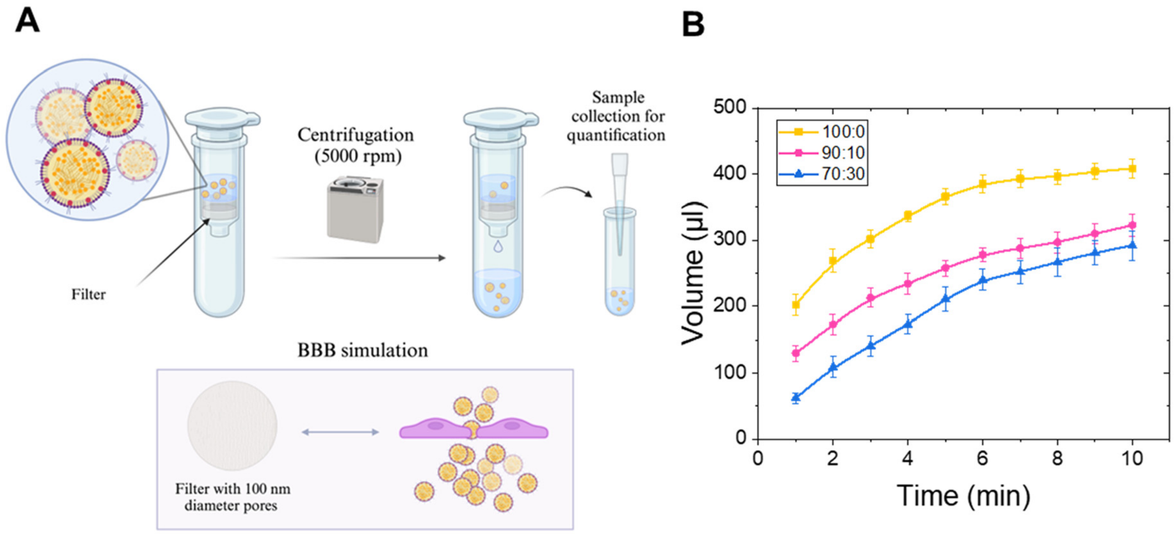

Fig. 5 Ultracentrifugation spin-down assay. (A) Schematic representation of the ultracentrifugation spin-down assay. (B) Passage of NLS through membranes over time $n = 3$.

Colloidal stability in biological media and biomolecular corona

Before proceeding to *in vitro* testing, the first step was to ensure that the NLSs remained stable in the culture medium used for the experiments. Given the lack of long-term stability exhibited by the 70 : 30 system (see colloidal stability section), which limits its potential for translational applications, only the 100 : 0 and 90 : 10 formulations were selected due to their superior stability. These two systems differed in mechanical properties and presented long-term stability, making them ideal for investigating whether these properties could influence cellular uptake and passage through a blood–brain barrier model while maintaining translational potential.

Therefore, the hydrodynamic diameter of the NPs was measured in serum-free DMEM (SF-DMEM) and DMEM (DMEM + FBS) supplemented with 10% FBS, and the results are shown in Fig. 6A and B. Notably, 90 : 10 NLSs exhibited little aggregation in serum-free DMEM during the studied time points, whereas 100 : 0 NLSs experienced minimal aggregation on the first day and remained stable until day 10. In line with previous results (Fig. 2), the presence of stearic acid in the core of the NLSs contributes to their increased instability. When both formulations were dispersed in DMEM with 10% FBS, aggregation did not occur, suggesting that protein adsorption onto the surface of the NLSs provides colloidal stability, probably due to the hydration forces generated.[21] The high stability of the 100 : 0 and 90 : 10 nanosystems in DMEM + FBS is of utmost importance, as it demonstrates that NLSs can maintain their colloidal stability under physiologically relevant conditions, thereby paving the way for their application in biomedicine. Then, the standard procedure to investigate the formation of a biomolecular corona onto the NLS surface when exposed to a biological milieu was pursued. The presence of the biomolecular corona was analyzed by determining the *Z*-potential and monitoring it as a function of pH. Results are shown in Fig. 6C and D. It is worth noting that, after incubation in a biological medium for 1 h (DMEM supplemented with 10% FBS), corona-NLSs complexes exhibited less negative surface charge values compared to bare NLSs, which were stably maintained across the entire pH range evaluated. Even positive values were observed at pH 4 for both NLSs studied, suggesting a bimolecular corona formation. This observation clearly indicates that the formation of such layer onto the NLS surface has a significant impact on the *Z*-potential. Moreover, for both bare and corona-NLS complexes, the more basic the pH, the more negative the *Z*-potential values. Our results align with previous findings indicating that proteins present in the medium can adsorb onto the surface of NPs, altering their surface charge.[37,38] With the perspective of applying NLSs for biological applications, researchers need to consider that the formation of the biomolecular corona will affect their stability, hydrodynamic behaviour, and interaction capabilities with cells and tissue.

Cellular uptake analysis using flow cytometry

Following an exhaustive characterization of the NLSs, their direct interaction with biological systems was tested. First, we investigated the cell viability of the NLSs to ensure they did not produce any toxic effects. Cell viability was assessed after 1 hour and 24 hours of incubation with the human GBM cell line U-87 MG, and the results are shown in Fig. 7A. No significant impact on cell viability was observed. Then, we investigated the cellular uptake of NLSs by GBM cells to evaluate whether the different mechanical properties of the systems could significantly impact cell entry and accumulation. To enable NLS tracking and visualization, we performed all biological assays using fluorescently labelled NLSs by encapsulating coumarin 6, following the protocol detailed in the

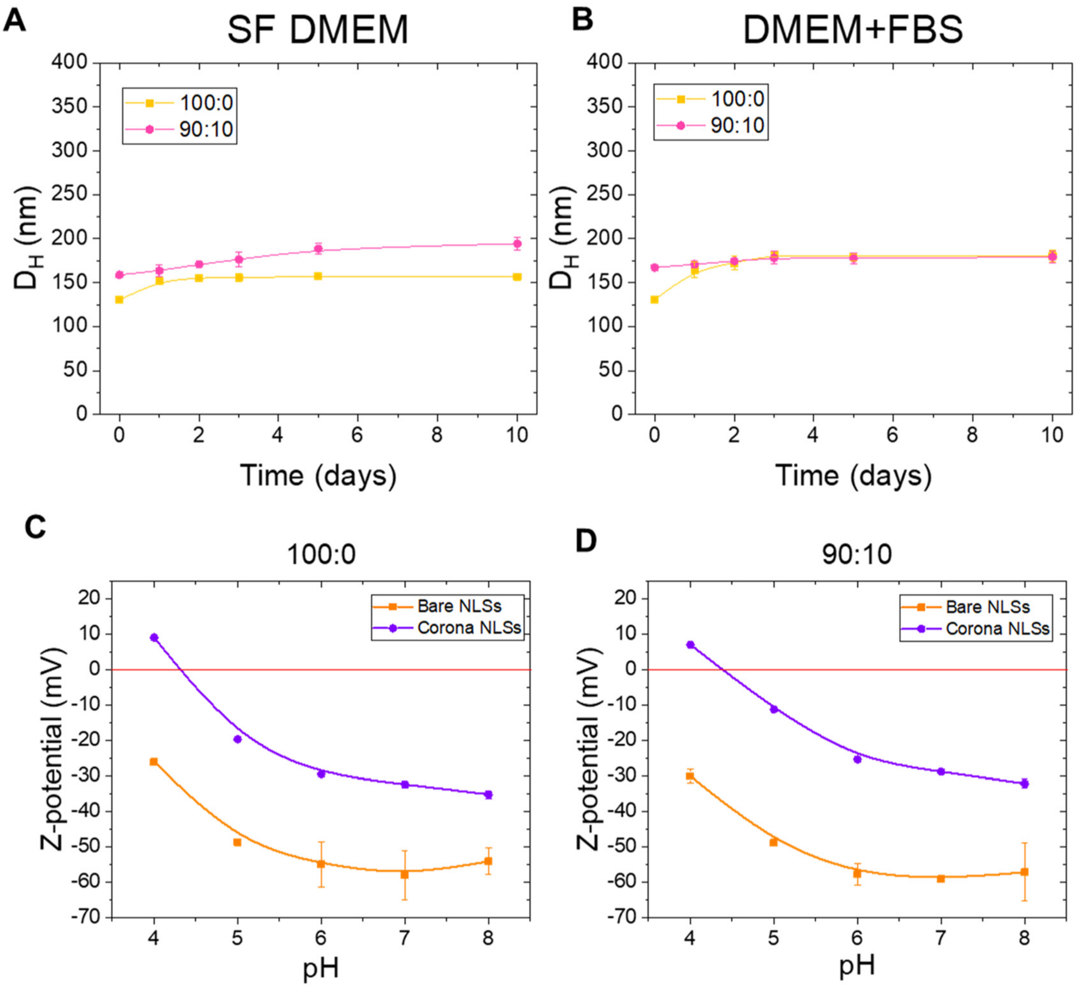

Fig. 6 Colloidal stability in biological media. (A) Evaluation of hydrodynamic mean diameter (D_H) as a function of time in serum free DMEM. (B) Evaluation of D_H as a function of time in DMEM + FBS. (C) *Z*-Potential as a function of pH for NLS 100 : 0 before (Bare NLSs) and after (Corona NLSs) incubation with DMEM + FBS. (D) *Z*-Potential as a function of pH for NLS 90 : 10 before (Bare NLSs) and after Incubation (Corona NLSs) with DMEM + 10%FBS. Error bars are included but are smaller than the data symbols, making them indistinguishable in some cases. Data are represented as the average of 3 independent replicates ± SD.

Materials and methods section. The successful encapsulation of coumarin 6 was confirmed through fluorescent measurements using a fluorometer, ensuring by DLS that the size and electric charge of the NLSs remained unaltered. Briefly, for the cellular uptake study, U-87 MG cells were exposed to the fluorescently labelled NLSs at a concentration of 1 × 10^{10} particles per ml, and their intracellular accumulation was evaluated at 30 minutes, 1 hour, 3 hours, and 24 hours. The results of this investigation are presented in Fig. 7B. Interestingly, 90 : 10 NLSs showed a higher uptake by the U-87 MG cells compared to 100 : 0 NLSs. This consistent trend was observed across all time points, indicating the significance of lipid composition in influencing cellular uptake behaviour. Given that both NLSs possess the same diameter, the specific observed behaviour can be attributed to their distinct mechanical properties, particularly the elastic modulus, suggesting that the amount of stearic acid in their core plays a critical role in shaping NLS cellular uptake characteristics. These results are in line with other publications that have studied the effect of rigidity on glioblastoma uptake with different nanomaterials,[39] as well as various works that investigated different cell line behaviours.[40] When comparing these results with those obtained with the spin-down assay (Fig. 5B) is seen that while 1000 : 0 NLSs demonstrate higher permeability through the filter tube, flow cytometry showed that 90 : 10 NLSs had higher uptake by cells. Nevertheless, it is important to note that these two experiments assess distinct biological effects: the centrifugation spin-down assay evaluates the ability of NLSs to cross biological barriers, while the flow cytometry experiment investigates their efficiency in being internalized by cells. Moreover, studies on how nanoparticle rigidity affects uptake efficiency have yielded mixed results,[41–44] largely due to variations in the cell types used. Additionally, deformability is influenced not only by the bending modulus of nanoparticles but also by their size and shape, making comparisons between nanoparticles with different dimensions and geometries more

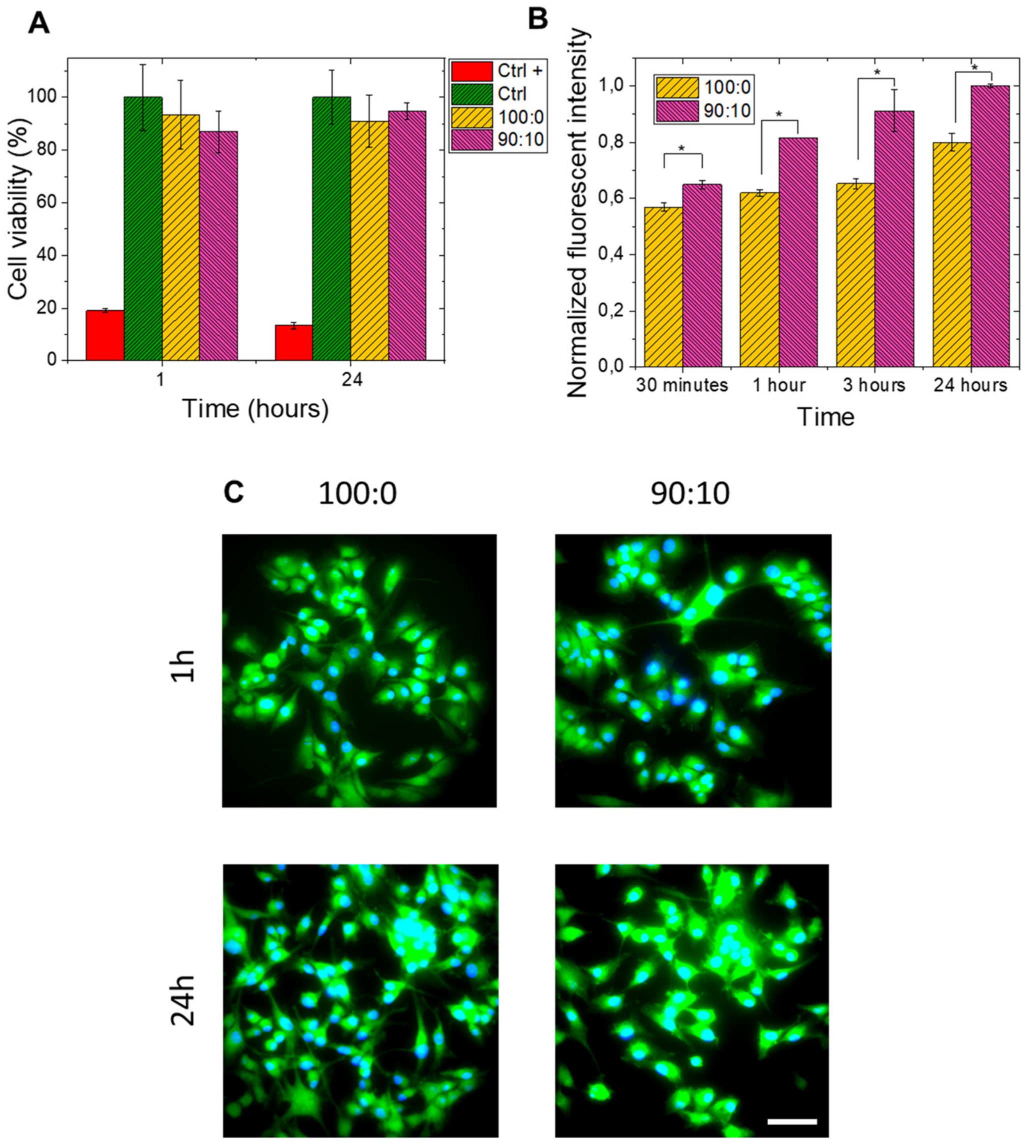

Fig. 7 Fluorescently- labelled NLS cell uptake. (A) MTT cell viability assay performed at 1 and 24 h. Ethanol 70% was used as a positive control. (B) Cellular uptake of NLS (100 : 0, and 90 : 10) at 30 min, 1 h, 3 h and 24 h. The SD is displayed (3 independent replicates). (C) Epifluorescence microscopy images of NLS cellular uptake (cell nuclei in blue and NLSs in green). Scale bar: 10 μm. Statically significative differences (T-student mean comparison test $*p < 0,05$).

complex.[40,45,45–47] In this regard, the system used in this study provides an advantage by allowing a direct comparison between two nanoparticles with similar size and shape but distinct mechanical properties.

In vitro blood–brain barrier transport assay

The two types of fluorescently-labelled NLSs (100 : 0 and 90 : 10) tested for cellular uptake were then exploited to evaluate their transport across an *in vitro* human model of blood–brain barrier (BBB). As detailed in Materials and methods, the concentration of NLSs (in percentage) that crosses the BBB was quantified according to time, making the measurement every hour for an interval of 4 hours. As characterized in the previous sections, these nanomaterials present similar sizes and morphological features but different core lipid structures (olive oil-stearic acid ratio) which results in different biomechanical behaviour. The BBB model that we employed was a monolayer culture of human brain microvascular endothelial cells (hCMEC/d3).[48,49] We followed the standard procedure of BBB formation to ensure the persistence of the barrier functionality and the tightness of the paracellular spaces.[48,49] Moreover, these parameters were also checked by TEER measurement before and after NLS exposure (Fig. S2†). Subsequently, we moved to investigate the capability of the NLSs to cross the BBB through transcellular transport. As the stability of the NLS dispersion is crucial in the processes of internalization and translocation, we only tested 100 : 0 and 90 : 0 systems. Cells were cultured on Transwell membranes with 3.0 μm pore size

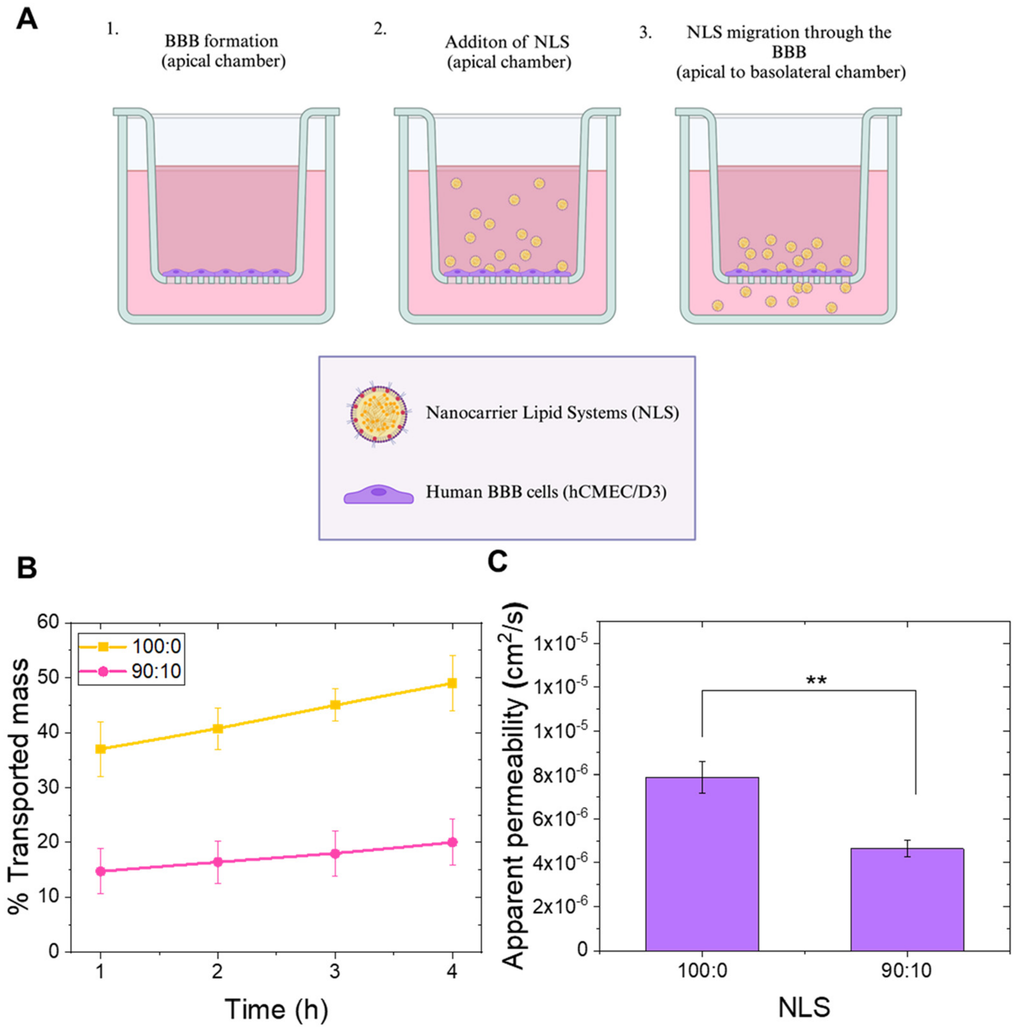

Fig. 8 NLS transport study across and *in vitro* human model of blood–brain barrier. (A) *In vitro* blood–brain barrier transport assay scheme. (B) Percentage of NLS crossing the BBB. (C) Apparent permeability of the NLS. The SEM is displayed (6 replicate measurements). Statically significative differences (T-student mean comparison test, $*p < 0.05$).

in the apical chamber of the Transwell device, and then incubated with 3×10^{10} particles per ml of 100 : 0 and 90 : 10 NLSs loaded in the apical chamber of the Transwell. As schematically shown in Fig. 8A, after 1, 2, 3, and 4 h of incubation on the apical side, a certain amount of NLSs should reach the basolateral side of the Transwell barrier. The results of the transported mass (in percentage normalized to the apical chamber initial concentration, Fig. 8B) show a higher passage of 100 : 0 NLSs compared to 90 : 10. In detail, more than 40% of the originally loaded 100 : 0 NLSs were able to reach the basolateral compartment, while in the case of the 90 : 10 NLS, only the 20% was found in the lower compartment after 4 h. Furthermore, an increase over time of the 100 : 0 NLSs can be seen, while 90 : 10 NLSs only present a slight tendency of active transport over time. These latest data were reflected and corroborated by also analysing the apparent permeability of such systems. Once again, the higher values were obtained for 100 : 0 compared to 90 : 10 (Fig. 8C), showing higher permeability and kinetics of the softer 100 : 0 NLSs. Such results are in alignment with the data from the ultracentrifugation spin-down assay (Fig. 5B) and suggest that 100 : 0 NLSs have a higher capability to be transported across biological barriers. TEER measurements also proved that these NLSs did not alter the integrity and functionality of BBB, showing a healthy interaction of the NLSs tested with the endothelium layer (Fig. S2†).

Materials and methods

Reagents

Poloxamer 188 (Pluronic F-68), stearic acid, and olive oil were purchased from Sigma-Aldrich (Merck Group, MN, USA). Epikuron 145 V was supplied by Cargill (MO, USA). Water was purified in a Milli-Q Academic Millipore system (Merck Group, MN, USA). Other solvents and chemicals used were purchased as specified in each section.

Cell line and culture conditions

U-87 MG human glioblastoma cell line was obtained from *Centro de Instrumentación Científica* (CIC) of Universidad de Granada (Spain). U-87 MG cells were cultured in Dulbecco's Modified Eagle's Medium (DMEM; Gibco, Thermo Fischer Scientific, MA, USA) supplemented with 10% (v/v) heat-inactivated fetal bovine serum (FBS; Gibco) and 1% penicillin/streptomycin (Gibco) solution. Cells were grown at 37 °C in an incubator containing 5% CO_2 and 95% humidity. Cells were tested routinely for mycoplasma contamination.

Synthesis of NLSs

NLSs were prepared using a modified solvent-displacement technique, as previously described by Sánchez-Moreno *et al.*[50] Briefly, an organic phase composed of 125 mg of a lipid mixture (olive oil and stearic acid in varying proportions of 100 : 0, 90 : 10, 70 : 30, 50 : 50 and 0 : 100), 40 mg of Epikuron 145 V dissolved in 1 ml of ethanol, and 9 ml of acetone were added vigorously to 20 ml of an aqueous phase containing 70 mg of Pluronic F68 under magnetic stirring. The organic solvents (acetone and ethanol) and a portion of the water volume were evaporated in a rotary evaporator at 37 °C, resulting in a volume of 15 ml with a final concentration of 15.6 mg ml^{-1}. The systems were then homogenised in a high-pressure homogeniser (Stansted Fluid Power, Pressure cell homogeniser, U.K.) at 100 MPa for ten cycles. For the preparation of fluorescent NLSs, 200 µl of coumarin-6 (Millipore, MA, USA) were dissolved in the organic phase at a concentration of 0.5 mg ml^{-1}.

Dynamic light-scattering analysis

The hydrodynamic mean diameter (D_H), polydispersity index (PDI), and surface zeta-potential (*Z*-Potential) of the NLSs were determined using a Zeta-Sizer Nano *Z* dynamic light-scattering analyser (Malvern Instruments, U.K.). For all measurements, the five NLS samples were diluted 100-fold in Milli-Q water, biological media (PBS, serum-free DMEM, DMEM-10% FBS), or low-ionic-strength (<2 mM) buffered solutions (pH 4, 5, 6, 7, and 8); subsequently, 1 ml of each sample was loaded into the disposable cuvette (or a folded-capillary zeta cell for *Z*-Potential acquisition) and measured (for each condition three independent runs were carried out). The scattered light from the samples was detected at 173° at 25 °C. The diffusion coefficient measured by dynamic light scattering was used to calculate the size of the NLSs by the Stokes–Einstein equation. PDI, which represents the homogeneity of the size distribution, was calculated from the analysis of the intensity autocorrelation function. Each data point was taken as an average over three independent sample measurements.

Nanoparticle tracking analysis

The size distribution of the NLSs was also evaluated by nanoparticle tracking analysis (NTA) using a NanoSight LM10-HS (GB) FT14 system with a sCMOS camera (NanoSight, Amesbury, UK). Furthermore, the particle concentration was calculated based on the size distribution of the NLSs, which was obtained from an average of at least three independent size distributions. The final concentration of NLS stocks was determined as 15.6 mg ml^{-1} for all NLSs (100 : 0, 90 : 10, 70 : 30, 50 : 50 and 0 : 100). The number of particles of 100 : 0, 90 : 10 and 70 : 30 NLSs was then calculated in order to perform biological experiments and exposed cells to the same amount of NLSs. Finally, for NTA analysis, stocks were diluted 1000-fold from the original concentration in deionized water. The measurements were performed at 25 °C, with viscosity of 1.0 cP, measurement time of 60 s, and camera gain of 250. The camera shutter was set to 15 ms. The detection threshold was fixed at 5.

Critical coagulation concentration (CCC) and critical stabilization concentration (CSC)

The CCC and CSC of the NLSs were determined by calculating the Fuchs factor (*W*), as previously described Peula-García *et al.*[51] using a Beckman DU 7400 spectrophotometer (Beckman Coulter, CA, USA) setting the wavelength at 570 nm. Briefly, 20 µl of the original concentration (15.6 mg mL^{-1}) of each NLSs were diluted in 1 ml of different concentrations of NaCl and $CaCl_2$ solutions and the absorbance was recorded every 3 seconds for 120 s and measured at 25 °C. From the analysis of aggregation kinetics, we calculated the CCC, defined as the minimum salt concentration needed for the most rapid aggregation, and the CSC related to the surface hydrophilicity and defined as the minimum salt concentration at which the system begins to re-stabilize when salinity is progressively increased.

Atomic force microscopy analysis

Atomic force microscopy (AFM) was used to investigate the bio-mechanical properties of the different NLSs synthesized. Samples were prepared by depositing a drop of 7 µl of each NLSs (100 : 0, 90 : 10, 70 : 30, 50 : 50 and 0 : 100) at the original concentration (15.67 mg ml^{-1}) onto a substrate of mica. The samples were let drying at RT and measured with NX20 AFM (Park Systems, South Korea). For non-contact mode analysis, ACTA cantilevers with a spring constant (*K*) of 40 N m^{-1} and a resonance frequency (f) of 320 kHz were used. Images were acquired with a 256 × 256 pixels resolution at a scan rate of 0.5–0.7 Hz. The obtained images were then processed and analysed using XEI software. Representative images of samples were obtained by scanning at least three different locations on three different samples for each NLS.

We used NSC-14 probes with a spring constant of 5 N m^{-1} and a resonance frequency of 160 kHz for Force Spectroscopy. The measurements were performed using the gentle PinPoint mode, which combines the horizontal and vertical movement of the tip in an approach-retract manner and allows for the application of forces of few nano-Newtons to preserve the sample. The software, simultaneously, acquires topographical data and each pixel's force–distance (F–D) curve. We obtained at least 30 force–distance (F–D) curves in each area only when the point was in contact with a nanoparticle. The values of stiffness, adhesion, and elastic modulus were obtained based on the study of F–D curves according to the specifications provided by Park Systems. Elastic modulus was given by the slope in the contact region of the F–D curve, adhesion by the minimum force in the curve, and stiffness was calculated from the displacement in F(nN) to tip indentation.

Rheology

Rheological measurements were conducted to characterize the mechanical properties of the NLS dispersed in water using a rotational rheometer Haake MARS III (Thermo Fisher Scientific, Waltham, MA, USA) at a temperature of 25 °C. We employed a 2° and 6 cm diameter titanium double cone geometry with smooth surfaces (Thermo Fisher Scientific, Waltham, MA, USA), which minimized wall slip effects. NLS were prepared for the experiments at a concentration of 40% v/v. Steady-state rheological measurements were performed, where the shear stress (σ) or viscosity (η) were measured as a function of the shear rate ($\dot{\gamma}$). In this case, the shear stress (σ) was varied from 1 to 4 Pa. Additionally, oscillatory shear amplitude sweeps and shear frequency sweeps, varying the strain amplitude (γ) from 0.01 to 5 at a constant angular frequency of 6.28 rad s^{-1}, and the angular frequency from 0.628 to 62.8 rad s^{-1} at constant strain amplitude of 0.1, respectively. From these tests, key rheological magnitudes such as the modulus of the complex viscosity (η^*) and the viscoelastic moduli (G' and G'') were obtained.

Biomolecular corona

To study the formation of biomolecular corona on NLSs, 10 µl of the original concentration (15.6 mg mL^{-1}) of each NLS (100 : 0, 90 : 10, 70 : 30, 50 : 50 and 0 : 100) were dispersed in 1 ml of a solution of complete DMEM supplemented with 10% FBS and incubated at 37 °C for 1 hour. The corona-NLS complexes were obtained by centrifuging the NLSs at 20 000g for 30 minutes at 4 °C to remove unbound proteins, followed by washing the resulting pellet with PBS. To analyse the changes in the colloidal properties of the corona-NLS complexes, the D_H, PDI, and Z-potential were determined in buffer solutions with pH values of 4, 5, 6, 7, and 8, as previously described.

Ultracentrifugation spin-down assay

The ultracentrifugation spin-down assay of NLSs was performed following the protocol previously described by Kong *et al.* 2021.[34] A total of 500 µl of the original concentration (15.67 mg ml^{-1}) of NLSs (100 : 0, 90 : 10, and 70 : 30) was carefully loaded into the upper filter compartment of a VIVASPIN 500 (Sartorius, UK) polyethersulfone (PES) ultracentrifuge tube fitted with a 100 nm diameter porous membrane. The tube was securely capped to prevent leakage during the centrifugation process. The loaded tube was then placed in an ultracentrifuge (Mikro 220R, Hettich) and centrifuged at 5000 rpm for 10 min. Subsequently, the volume of the filtrate passed through the pores was measured using a micropipette at 1 minute intervals over a total duration of 10 minutes.

Cellular uptake

Flow cytometry was used to assess the cellular biointeractions of NLS with U-87 MG cells. For this assay, 1.5 × 10^5 cells were seeded into 12-well culture dishes and treated with 3 × 10^{10} particles per mL of each type of coumarin-6-conjugated NLS (calculated from NTA data) at various time points (30 minutes, 1 hour, 3 hours, and 24 hours). After incubation, the NLS dispersion was removed, and the cells were washed twice with PBS. Cells were then detached using 0.05% Trypsin-EDTA in PBS for 5 minutes at 37 °C. The cell suspension was centrifuged at 500g for 5 minutes, and the cell pellet was resuspended in 300 µL of PBS. Flow cytometry analysis was performed using a FACSCanto II instrument (Becton Dickinson, New Jersey, US), and data were analyzed with FACSDiva 6.1.2 software (Becton Dickinson). Coumarin-6 fluorescence was used to quantify NLS uptake. Cells were gated using a forward scatter area *versus* side scatter area plot, and single cells were selected in a forward scatter height *versus* forward scatter area plot. At least 3 × 10^5 cells were acquired per sample.

Epifluorescence microscopy

U-87 MG cells were seeded at a concentration of 4 × 10^4 cells onto 12 mm Ø coverslips in 12-well culture dishes and treated with NLSs (100 : 0 and 90 : 10) at the same particle number concentration of 3 × 10^{10} part per ml for 1 and 24 hours. Cells were then fixed with 4% paraformaldehyde (Sigma Aldrich, MO, USA) in PBS for 15 min at RT. Samples were rinsed three times with PBS and incubated for 5 min with Hoechst (1 µM, Sigma Aldrich, MO, USA). Finally, samples were mounted on microscope slides using Mowiol (Sigma Aldrich, MO, USA). Image acquisitions were performed using inverted epifluorescence microscope (LEICA DM IRB, Leica Microsystems, Germany) equipped with 40x oil immersion objective (Leica Microsystems, Germany) and K5 cMOS microscope camera (Leica Microsystems, Germany). Images were processed with the open-source software ImageJ.

Cell viability

MTT viability assay was performed to assess the U-87 MG cell viability after NLS exposure and to discard any cytotoxic effect. Briefly, cells were seeded at 10^4 cells per well in a 96-well plate (Corning, Sigma-Aldrich, MI, USA). Cells were cultured for 24 h and then incubated with the different NLSs (100 : 0 and 90 : 10) for 1 and 24 hours at a concentration of 3 × 10^{10} particles per ml. After incubation, following the manufacturer's instructions, 20 µl of MTT reagent (CellTiter 96® AQueous One Solution Cell Proliferation Assay, PROMEGA, USA) were added to each well. Cells were incubated at 37 °C for 2 h and the absorbance values at 590 nm were measured using an Infinite M200 Nanoquant (Tecan, Switzerland) multimode microplate reader.

Human blood–brain barrier *in vitro* model

Cell culture. Immortalized human brain capillary endothelial cells (hCMEC/D3) were obtained from Cederlane Labs (Canada). For culturing, 5 × 10^4 cells were seeded in a 25 cm^3 flask (Becton Dickinson) and supplemented with

EBM-2 medium containing vascular endothelial growth factor (VEGF), insulin-like growth factor-1 (IL-1), epidermal growth factor (EGF), basic fibroblast growth factor (bFGF), fetal calf serum (2%), gentamicin sulfate/amphotericin B, and hydrocortisone, all sourced from Lonza Biosciences (NC, USA), as previously described.[48] Cells were cultured in an incubator at 37 °C with 5% CO_2 and 95% humidity. For experiments involving NLSs, cells were grown in EBM-2 complete medium during the monolayer formation process, which lasted seven days. Throughout this period, the cells were kept in an incubator at 37 °C under a 5% CO_2 and 95% air mixture with saturated humidity. To maintain cell health, the culture medium was replenished every two days, and the monolayer medium was refreshed twice weekly.

***In vitro* blood–brain barrier NLS transport assays.** To investigate the transport of NLSs across the *in vitro* blood–brain barrier model, 12-well plates with 0.1% gelatin pre-coated PTFE Transwell membrane inserts (3.0 µm of pore size and 1.12 cm of surface area;Corning, NY, USA) were used. hCMEC/D3 cells were seeded in the apical compartment of the Transwell membrane at a density of 4×10^4 cells per filter in 0.5 mL of EBM-2 medium. The basolateral compartment was filled with 1.5 mL of EBM-2 medium. Cell cultures were maintained for seven days after seeding on the Transwell to ensure the formation of a functional endothelial cell monolayer. Transport assays designed to assess the permeability of NLS across the *in vitro* blood–brain barrier model were performed by adding 0.5 mL of medium containing fluorescently-labeled NLSs (3×10^{10} particles per mL) to the apical compartment of the Transwell, while the basolateral compartment was filled with 1.5 mL of medium. The Transwell devices were then incubated at 37 °C with 5% CO_2/95% air and saturated humidity to simulate physiological conditions. At predefined intervals (1 hour), 100 µL samples were withdrawn from the basolateral compartment, with sampling continuing up to 4 hours. The removed 100 µL samples were replaced with fresh medium to maintain sink conditions. Fluorescence measurements of the samples were conducted using an Infinite M200 Nanoquant (Tecan, Switzerland) multimode microplate reader, with a 420 nm filter for excitation and fluorescence emission readings at 500 nm. Serial dilutions of NLS, ranging from 100% to 0.39% of the initial concentration loaded in the Transwell apical chamber, were prepared to generate a calibration curve for both NLSs tested (100 : 0 and 90 : 10). Linear regression was applied to establish the correlation between fluorescence intensity and NLS mass concentration, which was then used to determine the total mass of NLS in the basolateral chamber. The regression coefficients obtained from the linear curve fits were typically between 0.97 and 0.99 (n = 3 wells, from 2 independent culture preparations). The apparent permeability (P_{app}) of NLS was determined using the following equation:

$$P_{\mathrm{app}} = \frac{1}{A} C_0 \frac{\mathrm{d}Q}{\mathrm{d}t}$$

where A represents the surface area of the membrane in cm^2, C_0 is the initial concentration of NLS in the apical compartment (µg mL^{-1}), and dQ/dt is the amount of NLS that appears in the basolateral compartment in the given time period (µg s^{-1}). *trans*-Endothelial electrical resistance (TEER) measurements were performed on hCMEC/D3 monolayers using a CellZscopeE instrument (NanoAnalytics, Münster, Germany) before and after NLS transport studies to ensure the integrity of the cell monolayer upon NLS exposure.

Statistics

The results are expressed as the mean of at least three independent replicates, with the standard deviation. Both statistical analyses and graph generation were performed using Origin® software.

Conclusions

In this study, five different NLSs were successfully formulated by blending olive oil and stearic acid in varying proportions (100 : 0, 90 : 10, 70 : 30, 50 : 50, and 0 : 100), with 100 : 0 representing olive oil-core NLSs. Comprehensive characterization identified the 100 : 0 and 90 : 10 NLSs as the most promising candidates for biomedical applications, while the 50 : 50 and 0 : 100 systems exhibited high PDI values indicative of aggregation and instability. Although the 70 : 30 NLSs initially appeared viable for biological investigations, their colloidal instability over time rendered them unreliable for future applications.

Our findings demonstrate that tuning the NLS core lipid composition significantly influences their mechanical properties. NLSs with a pure olive oil core (100 : 0) exhibited a softer structure, while increasing the stearic acid content (90 : 10 and 70 : 30) enhanced rigidity. These mechanical differences notably impacted bio-interactions, particularly with biological barriers and cellular uptake. Softer 100 : 0 NLSs showed superior translocation across biological barriers, as confirmed by centrifugation spin-down assays and an *in vitro* human blood–brain barrier (BBB) model, highlighting their potential for cargo delivery to protected organs such as the brain. Conversely, glioblastoma cell uptake studies revealed that the more rigid 90 : 10 NLSs were internalized more efficiently by U87-MG cells, suggesting that increased stiffness may enhance cellular entry.

Given these results and considering that our NLSs were studied in their bare form (without additional surface functionalization), it is crucial to balance their mechanical properties to optimize both barrier penetration and targeted cellular uptake. Furthermore, although no therapeutic agents were encapsulated in the present formulations, these systems are intended for drug delivery applications, making it essential to evaluate the impact of drug incorporation on nanoparticle behavior. Since crossing biological barriers—particularly the BBB—remains a major challenge in nanomedicine and drug delivery for brain-related diseases, we propose 100 : 0 NLSs as the most promising candidates for further studies, including surface functionalization, to enhance drug delivery to the brain.

Author contributions

A.R.F. and D.J.B. participated in the design of the work, data acquisition, methodology and writing the original draft. A.L.C. contributed to the rheological data acquisition and interpretation. M.V.M. contributed to the synthesis of the NLSs. J.A.T, M.A.C. and A.M.R. contributed to the design of the work and helped with data interpretation. M.T.L.L. designed and supervised the rheological data and their interpretation. C.L.M.M. contributed to the conceptualization and design of the work, data interpretation and writing of the original draft. M.B and P.S.M designed and conceptualize the work, supervised the data acquisition and interpretation, contributed to write the original draft and are responsible for the project administration and funding resources. All authors contributed to critically review and approve the final version of the manuscript.

Data availability

The data supporting this article have been included as part of the ESI.†

Conflicts of interest

There are no conflicts to declare.

Acknowledgements

The authors acknowledge the funding provided by MCIN/AEI 10.13039/501100011033 through grant PID2021-124363OA-I00. D. Jiménez-Boland and A. Robles-Fernández wish to thank MCIU for their respective Ph.D. student fellowships (FPU22/01773 and PRE2022-103642, respectively). M. Bramini extends appreciation for support under the Ramón y Cajal program (MCIU/AEI, RYC2019-027692-I). A. León-Cecilla acknowledges grants FPU19/01801 funded by MCIN/AEI/10.13039/501100011033 and "ESF Investing in your future", Spain.

Finally, the authors express their gratitude to the Scientific Instrumentation Centre (CIC) at the University of Granada for their valuable technical assistance.

References

1 J. K. Patra, G. Das, L. F. Fraceto, E. V. R. Campos, M. D. P. Rodriguez-Torres, L. S. Acosta-Torres, L. A. Diaz-Torres, R. Grillo, M. K. Swamy, S. Sharma, S. Habtemariam and H. S. Shin, *J. Nanobiotechnol.*, 2018, **16**, 71.

2 F. Rehan, M. Zhang, J. Fang and K. Greish, *Molecules*, 2024, **29**, 1–28.

3 J. L. Andresen and O. S. Fenton, *MRS Bull.*, 2021, **46**, 832–839.

4 S. Wilhelm, A. Tavares, Q. Dai, S. Ohta, J. Audet, H. F. Dvorak and W. C. W. Chan, *Nat. Rev. Mater.*, 2016, **1**, 16014.

5 T. Moraes-Lacerda and M. Jesus, *Collloids Surf B: Biointerfaces*, 2022, **220**, 112863.

6 P. Graván, A. Aguilera-Garrido, J. A. Marchal, S. A. Navarro-Marchal and F. Galisteo-González, *Adv. Colloid Interface Sci.*, 2023, **314**, 102871.

7 P. Sánchez-Moreno, J. L. Ortega-Vinuesa, A. Martín-Rodríguez, H. Boulaiz, J. A. Marchal-Corrales and J. M. Peula-García, *Int. J. Mol. Sci.*, 2012, **13**(2), 2405–2424.

8 J. Szafraniec-Szczęsny, M. Janik-Hazuka, J. Odrobińska and S. Zapotoczny, *Polymers*, 2020, **12**, 1–25.

9 H. A. Mohammed, R. A. Khan, V. Singh, M. Yusuf, N. Akhtar, G. M. Sulaiman, S. Albukhaty, A. A. H. Abdellatif, M. Khan, S. A. A. Mohammed and A. M. Al-Subaiyel, *Nanotechnol. Rev.*, 2023, **12**, 20220517.

10 Y. Hui, X. Yi, F. Hou, D. Wibowo, F. Zhang, D. Zhao, H. Gao and C.-X. Zhao, *ACS Nano*, 2019, **13**(7), 7410–7424.

11 L. Zhang, Z. Cao, Y. Li, J. R. Ella-Menye, T. Bai and S. Jiang, *ACS Nano*, 2012, **6**, 6681–6686.

12 Y. Hui, D. Wibowo, Y. Liu, R. Ran, H. F. Wang, A. Seth, A. P. J. Middelberg and C. X. Zhao, *ACS Nano*, 2018, **12**, 2846–2857.

13 Z. Shen, H. Ye and Y. Li, *Phys. Chem. Chem. Phys.*, 2018, **20**, 16372–16385.

14 X. Yi and H. Gao, *Nanoscale*, 2017, **9**, 454–463.

15 P. Gurnani, C. Sanchez-Cano, H. Xandri-Monje, J. Zhang, S. H. Ellacott, E. D. H. Mansfield, M. Hartlieb, R. Dallmann and S. Perrier, *Small*, 2022, **18**, 2203070.

16 P. Sánchez-Moreno, H. Boulaiz, J. L. Ortega-Vinuesa, J. M. Peula-García and A. Aránega, *Int. J. Mol. Sci.*, 2012, **13**(4), 4906–4919.

17 C. Farace, P. Sánchez-Moreno, M. Orecchioni, R. Manetti, F. Sgarrella, Y. Asara, J. M. Peula-García, J. A. Marchal, R. Madeddu and L. G. Delogu, *Sci. Rep.*, 2016, **6**, 18423.

18 J. Dolai, K. Mandal and N. R. Jana, *ACS Appl. Nano Mater.*, 2021, **4**, 6471–6496.

19 P. Sánchez-Moreno, J. L. Ortega-Vinuesa, H. Boulaiz, J. A. Marchal and J. M. Peula-García, *Biomacromolecules*, 2013, **14**(12), 4248–4259.

20 N. Kathe, B. Henriksen and H. Chauhan, *Drug Dev. Ind. Pharm.*, 2014, **40**, 1565–1575.

21 J. A. Molina-Bolívar and J. L. Ortega-Vinuesa, *Langmuir*, 1999, **15**, 2644–2653.

22 D. M. Smith, J. K. Simon and J. R. Baker, *Nat. Rev. Immunol.*, 2013, **13**, 592–605.

23 P. K. Parikh, N. H. Parikh, J. K. Patel and Y. V. Pathak, *Pharmacokinet. Pharmacodyn. Nanoparticulate Drug Deliv. Syst*, 2022, pp. 315–331.

24 Z. Zhao, A. Ukidve, J. Kim and S. Mitragotri, *Cell*, 2020, **181**, 151–167.

25 P. Guo, D. Liu, K. Subramanyam, B. Wang, J. Yang, J. Huang, D. T. Auguste and M. A. Moses, *Nat. Commun.*, 2018, **9**, 1–9.

26 R. Jeitler, C. Glader, G. König, J. Kaplan, C. Tetyczka, J. Remmelgas, M. Mußbacher, E. Fröhlich and E. Roblegg, *Mol. Pharm.*, 2024, **21**, 3674–3683.

27 A. Beloqui, M.Á Solinís, A. Rodríguez-Gascón, A. J. Almeida and V. Préat, *Nanomed. Nanotechnol. Biol. Med.*, 2016, **12**, 143–161.

28 C. Jin, Q. Wu, G. Yang, H. Zhang and Y. Zhong, *Powder Technol.*, 2021, **389**, 1–10.

29 M. Liu, F. Wang, C. Pu, W. Tang and Q. Sun, *Food Chem.*, 2021, **358**, 129840.

30 J. Mewis, W. J. Frith, T. A. Strivens and W. B. Russel, *AIChE J.*, 1989, **35**, 415–422.

31 H. A. Barnes, J. F. Hutton and K. Walters, *An Introduction to Rheology*, Elsevier Science, 1989.

32 C. H. Albertsen, J. A. Kulkarni, D. Witzigmann, M. Lind, K. Petersson and J. B. Simonsen, *Adv. Drug Deliv. Rev.*, 2022, **188**, 114416.

33 A. E. Nel, L. Mädler, D. Velegol, T. Xia, E. M. V. Hoek, P. Somasundaran, F. Klaessig, V. Castranova and M. Thompson, *Nat. Mater.*, 2009, **8**, 543–557.

34 S. M. Kong, D. F. Costa, A. Jagielska, K. J. Vliet and P. T. Hammond, *Proc. Natl. Acad. Sci. U.S.A.*, 2021, **118**(42), e2104826118.

35 K. Greish, Cancer Nanotechnology, in *Methods in Molecular Biology*, Humana Press, 2010, vol. 624.

36 M. D. Sweeney, K. Kisler, A. Montagne, A. W. Toga and B. V. Zlokovic, *Nat. Neurosci.*, 2018, **21**, 1318–1331.

37 P. Graván, J. Peña-Martín, J. L. de Andrés, M. Pedrosa, M. Villegas-Montoya, F. Galisteo-González, J. A. Marchal and P. Sánchez-Moreno, *ACS Appl. Mater. Interfaces*, 2024, **16**, 2058–2074.

38 P. Sánchez-Moreno, P. Buzón, H. Boulaiz, J. M. Peula-García, J. L. Ortega-Vinuesa, I. Luque, A. Salvati and J. A. Marchal, *Biomaterials*, 2015, **61**, 266–278.

39 C.-F. Kuo, F. Mirab, M. R. Abidian and S. Majd, in 2022 44th Annual International Conference of the IEEE Engineering in Medicine & Biology Society (EMBC), IEEE, Glasgow, Scotland, United Kingdom, 2022, pp. 3927–3930.

40 T. Stern, I. Kaner, N. Laser Zer, H. Shoval, D. Dror, Z. Manevitch, L. Chai, Y. Brill-Karniely and O. Benny, *J. Controlled Release*, 2017, **257**, 40–50.

41 D. Montizaan, C. Saunders, K. Yang, S. Sasidharan, S. Maity, C. Reker-Smit, M. C. A. Stuart, C. Montis, D. Berti, W. H. Roos and A. Salvati, *Small*, 2023, **19**, 2303267.

42 W. Liu, X. Zhou, Z. Mao, D. Yu, B. Wang and C. Gao, *Soft Matter*, 2012, **8**, 9235.

43 A. C. Anselmo, M. Zhang, S. Kumar, D. R. Vogus, S. Menegatti, M. E. Helgeson and S. Mitragotri, *ACS Nano*, 2015, **9**, 3169–3177.

44 J. Sun, L. Zhang, J. Wang, Q. Feng, D. Liu, Q. Yin, D. Xu, Y. Wei, B. Ding, X. Shi and X. Jiang, *Adv. Mater.*, 2015, **27**, 1402–1407.

45 Z. Shen, H. Ye, X. Yi and Y. Li, *ACS Nano*, 2019, **13**, 215–228.

46 R. Palomba, A. L. Palange, I. F. Rizzuti, M. Ferreira, A. Cervadoro, M. G. Barbato, C. Canale and P. Decuzzi, *ACS Nano*, 2018, **12**, 1433–1444.

47 Y. Hui, X. Yi, F. Hou, D. Wibowo, F. Zhang, D. Zhao, H. Gao and C.-X. Zhao, *ACS Nano*, 2019, **13**, 7410–7424.

48 M. Bramini, D. Ye, A. Hallerbach, M. Nic Raghnaill, A. Salvati, C. Åberg and K. A. Dawson, *ACS Nano*, 2014, **8**, 4304–4312.

49 M. N. Ragnaill, M. Brown, D. Ye, M. Bramini, S. Callanan, I. Lynch and K. A. Dawson, *Eur. J. Pharm. Biopharm.*, 2011, **77**, 360–367.

50 P. Sánchez-Moreno, J. L. Ortega-Vinuesa, A. Martín-Rodríguez, H. Boulaiz, J. A. Marchal-Corrales and J. M. Peula-García, *Int. J. Mol. Sci.*, 2012, **13**, 2405–2424.

51 J. M. Peula-García, J. L. Ortega-Vinuesa and D. Bastos-González, *J. Phys. Chem. C*, 2010, **114**, 11133–11139.